Andrea Giuliani, Vadim S. Kamenetsky, Mark A. Kendrick, David Phillips and Karsten Goemann

Nickel-rich metasomatism of the lithospheric mantle by pre-kimberlitic alkali-S-Cl-rich C-O-H fluids

Andrea Giuliani*, Mark A. Kendrick, David Phillips
School of Earth Sciences, The University of Melbourne, Parkville, 3010 Victoria, Australia
* corresponding author; email: a.giuliani@student.unimelb.edu.au
ph: 0061-3-83447672; fax: 0061-3-83447761

Vadim S. Kamenetsky
ARC Centre of Excellence on Ore Deposits and School of Earth Sciences, University of Tasmania, Hobart, Australia

Karsten Goemann
Central Science Laboratory, University of Tasmania, Hobart, Australia

Abstract Metasomatism of the lithospheric mantle sometimes produces unusual assemblages containing native metals and alloys, which provide important insight into metasomatic processes in the mantle. In this study, we describe the metasomatic enrichment of a refractory harzburgite xenolith in Ni, Fe and, to a lesser extent, Cu, Co, As and Sb. The xenolith (XM1/422) derives from the Bultfontein kimberlite (Kimberley, South Africa) and hosts Ni mineralisation that includes native nickel ($Ni_{84.5-98.0}$), heazlewoodite (Ni_3S_2) and Ni-rich silicates (e.g. up to 37.5 wt.% NiO in olivine, and 22.4 wt.% NiO in phlogopite). The presence of several mineral phases enriched in alkali and volatile species (e.g. phlogopite, phosphates, carbonates, chlorides, djerfisherite) indicates that the transition metal cations were likely introduced during metasomatism by alkali-rich C-O-H fluids or alkali carbonate melts. It is postulated that sulphide breakdown and fluid reaction with refractory mantle rocks contributed to the fluid's enrichment in Ni and other metallic cations. The Ni-rich assemblages of xenolith XM1/422 show local chemical disequilibrium, and modelling of the Ni diffusion profiles adjacent to olivine-native nickel and olivine-heazlewoodite grain boundaries, suggests a close temporal relationship

between Ni-rich metasomatism and subsequent entrainment by the kimberlite magma. However, metal-rich metasomatism also occurs in domains of the lithospheric mantle, including orogenic peridotitic massifs and the sub-oceanic lithospheric mantle, which were not affected by kimberlite magmatism. As micro-scale occurrences of metallic phases are easily overlooked, it is possible that metal-rich metasomatism is more widespread in the Earth's mantle than previously recognised.

Keywords native nickel; olivine; metasomatism; C-O-H fluids; lithospheric mantle; kimberlite

Introduction

Native metals and alloys present in the lithospheric mantle can have a variety of origins: i) they can occur as refractory phases after partial melting of fertile peridotites (Lorand et al. 2010; Luguet et al. 2007), ii) derive from desulphidation or low-T recrystallisation of sulphides (Keays et al. 1981; Lorand et al. 2010), iii) or precipitate from metal-rich fluids that interact with silicate minerals (Ishimaru et al. 2009; Jacob et al. 2004). Therefore, geochemical and micro-textural studies of metallic minerals, and accompanying phases in mantle xenoliths provide an important means to document the chemical features of associated mantle fluids (Alard et al. 2011; Lorand and Alard 2001; Lorand et al. 2010).

Mantle xenoliths entrained by kimberlites and related magmas display metasomatic alteration by fluids of variable composition. In this context, the term 'fluid' covers 'melts' as well as 'fluids' composed of C-O-H volatile species that contain variable dissolved silicate or carbonate components (e.g. Harte, 1987). The specific term 'melt' is only applied when the fluid composition is established to be overwhelmingly silicate and/or carbonate. Important metasomatic agents include C-O-H fluids (Andersen et al. 1984; Frezzotti et al. 2010), alkali-basaltic melts (Burgess and Harte 2004), carbonate-rich melts (Giuliani et al. 2012; Yaxley et al. 1998), and kimberlitic melts (Kinny and Dawson 1992). Carbonate and silicate melts can effectively transfer base and precious metal cations through the Earth's mantle (Fiorentini and Beresford 2008; Garuti et al. 1997; Lorand et al. 1993 and 2004), but usually at low concentrations. Sulphide melts are the most efficient carriers of

chalcophile metal cations (e.g. Ni, Cu, Pd) in the mantle. However, sulphide liquids can only migrate after coexisting silicate melts have completely crystallised (Mungall and Su 2005); and the wetting ability (i.e. mobility) of mantle sulphide melts depends on oxygen fugacity conditions (Gaetani and Grove 1999), and melt composition (Rose and Brenan 2001). Finally, C-O-H fluids can efficiently transport metallic cations in solution if the fluids are enriched in Cl and S (e.g. Fleet and Wu 1995; Lorand et al. 2004), because these volatile elements form ligands (e.g. chloride, bisulphide) that complex with metallic cations.

During the petrologic investigation of a suite of metasomatised mantle xenoliths from the Bultfontein Kimberlite (Kimberley, South Africa), we found an atypical Ni mineralisation occurrence in a sample of spinel harzburgite (XM1/422). The Ni mineralisation includes native nickel, heazlewoodite (Ni_3S_2) and silicates with extreme Ni enrichment. Similar Ni-rich mineralisation has been identified in other xenoliths from the Kaapvaal craton lithospheric mantle sampled by kimberlite magmas (Lorand and Gregoire 2006) as well as from mantle wedge xenoliths (Ishimaru and Arai 2008), and native nickel has been previously detected as inclusions in diamonds (Harte 2012) and in olivine from mantle wedge peridotites (Ishimaru et al. 2009). In this paper we detail the petrology of the Ni mineralisation present in xenolith XM1/422 and examine the unusual mantle metasomatic processes that produced native nickel and minerals enriched in Ni, Fe, alkalis, volatiles and chalcophile elements. Our findings indicate that alkaline, volatile-rich metasomatic fluids in the lithospheric mantle are capable of mobilising significant quantities of base metal cations, in accord with experimental simulations (Fleet and Wu 1995; Wood et al. 1987).

Geological Setting

The Bultfontein Kimberlite is part of the Kimberley cluster of kimberlites, which is located on the Kaapvaal craton, and has been dated at 84 ± 3 Ma using various isotopic systems (e.g. phlogopite Rb/Sr - Allsopp and Barrett 1975). The Kimberley kimberlites are classified as Group I kimberlites on the basis of their Sr-Nd isotope signatures (Smith 1983). The Kimberley kimberlites are renowned for hosting mantle xenoliths characterised by distinct metasomatic styles (e.g. MARID and related rocks, glimmerites, PIC rocks, polymict peridotites - Field et al. 2008; Pearson et al. 2003, and references therein).

Analytical techniques

Thin sections obtained from different parts of xenolith XM1/422 were characterised in transmitted light using a Nikon Labophot 2-Pol petrographic microscope. The textural relationships and phase compositions of the Ni-rich areas were subsequently investigated in more detail using a Scanning Electron Microscope (SEM) and Electron Microprobe (EMP).

Scanning electron microscopy was undertaken on thin sections polished without using water in order to preserve water-soluble minerals. SEM investigations were initiated at the University of Melbourne using a Philips (FEI) XL30 ESEM TMP equipped with an OXFORD INCA energy-dispersive x-ray spectrometer (EDS). Scanned EDS images of the whole thin sections were obtained using the FEI Quanta MLA ESEM located at the Central Science Laboratory, University of Tasmania. A more detailed study of the Ni mineralisation was performed on the same thin sections at the Central Science Laboratory, University of Tasmania using a Hitachi SU-70 field emission scanning electron microscope (FE-SEM) equipped with an OXFORD INCA-XMax80 EDS. The ultra-high resolution FE-SEM enables imaging of nm-sized surface features in secondary electron mode. A beam acceleration voltage of 15 kV was utilised for imaging and standardless, semi-quantitative EDS chemical analyses and elemental mapping.

Major oxide analyses were performed using a Cameca SX50 Electron Microprobe located at the University of Melbourne, and a Cameca SX100 Electron Microprobe hosted at the Central Science Laboratory, University of Tasmania. The Cameca SX50 is equipped with four, the Cameca SX100 with five vertical Wavelength Dispersive Spectrometers (WDS). The analytical conditions were as follows: beam acceleration voltage of 15 kV for silicate and oxide minerals and 20 kV for sulphides and native metals, beam current between 15 and 40 nA, and beam diameter between 0.8 and 5.0 μm, depending on mineral size. The detection limits are ~300 ppm for most elements.

The trace element concentrations of olivine and orthopyroxene from the spinel harzburgite were measured by laser ablation ICP-MS using an Agilent 7700X quadrupole ICP-MS located at the University of Melbourne. The instrument is interfaced to an excimer 193 nm UV laser ablation probe for in situ analyses of minerals (see Woodhead et al., 2007, for a detailed description of analytical procedures). Laser ablation conditions for the current study were as follows: ablation times of 40 s; repetition rate of 5 Hz; standard delay for sample washout of 20 seconds; longer delays for background measurements (60 seconds) every 8 analyses, and at the beginning and end of each analytical session; beam size of 72 μm. The isotopes monitored include ^{7}Li, ^{23}Na, ^{25}Mg, ^{29}Si ^{43}Ca, ^{45}Sc, ^{49}Ti, ^{51}V, ^{52}Cr, ^{59}Co, ^{60}Ni, ^{63}Cu, ^{66}Zn and ^{98}Mo. The synthetic glass NIST612 (with concentrations taken from Jochum and Stoll 2008) was used as the calibration standard, and ^{25}Mg as the internal standard. Natural and synthetic glasses BCR-2G and NIST610 were employed as external standards for checking the quality of results.

Petrography

Spinel harzburgite

Sample XM1/422 is an off-cut (2×3×3 cm; Figs. 1 and 1EA) of a larger spinel harzburgite xenolith with coarse granular texture. Olivine (hereafter 'porphyroblastic olivine') occurs as large (2-8 mm) grains and is slightly more abundant than orthopyroxene. Orthopyroxene forms two distinct populations: coarse-grained crystals ('porphyroblastic orthopyroxene') comparable in size to the olivine, and smaller grains ('interstitial orthopyroxene') that occur interstitially to porphyroblastic olivine and orthopyroxene. The different generations of the major silicate and oxide minerals distinguished in the xenolith are summarised in Table 1. The porphyroblastic olivine and orthopyroxene have been serpentinised along the edges and cracks likely at high temperature, after xenolith emplacement in the upper crust. Chrome-rich spinel is less abundant (< 5 vol%), and is intergrown with variable amounts of fine-grained clinopyroxene (diopside) and orthopyroxene ('symplectitic'; Fig. 2a). In some areas the spinel + pyroxene symplectites are altered to phlogopite and spinel ('altered Ni-poor spinel'; Fig. 2b) along margins. In these marginal zones spinel hosts abundant micro-inclusions of phlogopite, Ca-Na-Mg phosphates (apatite and bradleyite), dolomite, alkali carbonates, and minor chlorides and Ni-Fe sulphides (identified by SEM-EDS analyses; Online Resource Figs. 3EA, 4EA).

Nickel-rich mineralisation

Nickel-rich assemblages (Figs. 2c-f, 3 and 2EA, 3EA) represent between 0.15 and 0.25 vol% of the xenolith (estimated using scanned EDS images of the thin sections). They are located interstitially with respect to porphyroblastic olivine and orthopyroxene grains, and are associated with locally intergrown grains of spinel, diopside and less frequent orthopyroxene (Figs. 2c, 2d, 2f). About half the Ni-rich assemblages consist of relatively large (up to 200 μm) grains of native nickel (Fig. 2c), heazlewoodite (Ni_3S_2; Fig. 2e) and rare djerfisherite [$K_6Na(Fe,Cu,Ni)_{25}S_{26}Cl$], with the remainder composed of fine-grained granoblastic domains dominated by 'Ni-

Fe-rich olivine' (Table 1; Fig. 3). The native nickel grains are homogeneous, free of inclusions and mantled by either heazlewoodite or a thin irregular layer of finely intergrown heazlewoodite and magnetite, the latter likely produced during serpentinisation of the xenolith after emplacement in an upper crustal environment. The large grains of heazlewoodite host small (< 5 μm) inclusions of native copper, Cu-sulphide (Fig. 4a) and Sb-bearing gersdorffite (NiAsS; Fig. 3d), the latter likely representing a low-T exsolution feature. Some heazlewoodite grains contain abundant often elongated (flame-like) inclusions of Ni-Co-rich pentlandite (Fig. 4a) that likely exsolved with decreasing temperature. Heazlewoodite also forms thin veins that rim the Ni-rich assemblages.

The fine-grained granoblastic domains of Ni-Fe-rich olivine (Fig. 3) also contain Ni-Fe-rich fine-grained spinel, Ni-Fe-rich clinopyroxene, interstitial heazlewoodite and Ni-rich phlogopite, and minor apatite and aegirine. These domains are up to 100 μm in size, and have a granular texture due to the subhedral habit of Ni-Fe-rich olivine. Nickel-Fe-rich olivine hosts inclusions (< 2 μm) of Ni-Fe-rich spinel (Fig. 3e), heazlewoodite, Ni-Fe-rich clinopyroxene and minor Ti-bearing spinel, apatite, alkali-carbonate and calcite (Figs. 3EA, 6EA). Phlogopite hosts inclusions (< 1 μm) of Ni-Fe-rich olivine, Ni-Fe-rich spinel and heazlewoodite (Fig. 3f).

The Ni-rich assemblages include large (up to 150-200 μm) grains of spinel that are interpreted to have a relict origin ('relict spinel'; Table 1). These relict spinel grains are commonly associated with diopside (Fig. 2c) and have areas enriched in Ni, Fe and sometimes Ti (Fig. 4b), which are locally intergrown with heazlewoodite (Fig. 4c). The enriched areas of individual relict spinel grains host inclusions of phosphates (apatite and bradleyite), alkali-carbonates, Ni- and Cu-sulphide (Fig. 4d) and chlorides (halite and sylvite); and small (≤ 1.5 μm) homogeneous glass inclusions displaying negative crystal shapes of the host spinel (Figs. 4e, 7EA).

Small (< 10 μm large) grains of native nickel and heazlewoodite are occasionally included in the rims of porphyroblastic olivine (Fig. 4f) adjacent to the Ni-rich assemblages.

Mineral chemistry

Spinel harzburgite

Representative electron microprobe and LA-ICP-MS data documenting the composition of the dominant silicate phases in spinel harzburgite XM1/422 are reported in Tables 2 and 3. Porphyroblastic olivine grains have uniform major element compositions, characterised by Mg# between 92.3 and 92.7 [Mg# = 100×Mg/(Mg+Fe+Ni) atomic], and NiO between 0.30 and 0.40 wt.% (Fig. 5). Porphyroblastic olivine grains display core to rim depletion in Ca, Cr and to a lower extent Na (Table 3).

Porphyroblastic orthopyroxene (Mg# = 93.2±0.1 [1σ]) is in chemical equilibrium with porphyroblastic olivine, and has the same composition as the finer-grained interstitial orthopyroxene (Table 2). The rims of porphyroblastic orthopyroxene approach the composition of symplectitic orthopyroxene, which is slightly richer in Fe and Mg, and poorer in Ca and Al than the cores of porphyroblastic orthopyroxene. In terms of trace elements, the rims of porphyroblastic orthopyroxene are depleted in Cr, Ni, Co and Li compared to the cores. Symplectitic diopside contains low levels of Na_2O (< 0.6 wt.%).

Symplectitic spinel (Table 4) in the areas not affected by Ni enrichment is Mg-Al chromite with Cr# [=Cr/(Cr+Al+Fe^{3+})] between 0.55 and 0.58, and Mg# between 58 and 64. The Fe^{3+}/Fe_{tot} ratios are lower than 0.1, and the NiO concentrations are very low (< 0.07 wt.%; Fig. 6a). In the altered margins of spinel + pyroxene symplectites, the altered Ni-poor spinel is depleted in Al_2O_3 and MgO, and has higher Fe^{3+}/Fe_{tot} ratio than symplectitic spinel. The associated phlogopite ('Ni-poor'; Table 5) has variable composition (e.g. TiO_2 = 0.16-1.30 wt.%; Cr_2O_3 = 1.2-1.7 wt.%), but NiO is low (< 0.27 wt.%).

Nickel-rich mineralisation

Most phases in the Ni mineralisation display highly variable compositions. Native nickel grains contain variable amounts of Fe (1.3-13.8 wt.%; Table 6), and minor Co and Cu, although individual grains have very uniform compositions. The large grains of heazlewoodite have very low Fe (≤ 3.1 wt.%; Table 6) and minor Co and Cu impurities. Semi-quantitative EDS analyses of Ni-Co-rich pentlandite included in

heazlewoodite yielded Ni and Co contents between 38.4-44.9 and 12.5-16.2 wt.% respectively (Fig. 5EA; Table 1EA).

The composition of fine-grained Ni-Fe-rich olivine is much richer in NiO and FeO than porphyroblastic olivine (Fig. 5, Table 2). NiO varies between 13.1 and 37.4 wt.% and FeO between 7.4 and 20.1 wt.%. The grains most enriched in NiO approach the composition of the Ni-olivine end-member, liebenbergite (Fig. 5; de Waal and Calk 1973).

The Ni-Fe-rich clinopyroxene grains exhibit highly variable compositions, even within single grains, from similar to symplectite diopside, but with a distinct enrichment in NiO, to diopside enriched in Fe, Ni, Cr and Na (Table 2). The aegirine in the fine-grained domains contains up to 1.9 wt.% NiO (Table 2).

In the Ni-rich assemblages the grains of relict spinel have compositions varying from that of symplectitic spinel, to highly enriched in NiO, FeO_{tot}, Fe_2O_3 and TiO_2 (Table 4; Fig. 6). The Ni-Fe-rich fine-grained spinel is characterised by higher FeO_{tot}, Fe^{3+}/Fe_{tot}, and NiO (0.8-6.7 wt.%), and lower Al_2O_3 and MgO contents than the symplectitic spinel.

The composition of Ni-rich phlogopite varies in different Ni-rich assemblages (Table 5). In some Ni-rich regions the phlogopite is extremely enriched in NiO (up to 22.4 wt.%), and depleted in MgO, with high amounts of Na_2O and Cl. In other areas the phlogopite grains are less enriched in NiO (up to 1.9 wt.%), but display elevated Cr_2O_3 and TiO_2 contents.

EDS analyses of apatite reveal high concentrations in F or Cl. The sulphide djerfisherite is chlorine-free with no detectable Cu; the K content (5.6 wt.%; measured by EDS) of djerfisherite is much lower than commonly reported values (8.9-9.4 wt.%; Sharygin et al. 2007), due to post-emplacement alteration or alkali loss during electron beam ablation. The glass inclusions contained in the enriched relict spinel grains (Fig. 4e) show silicate compositions (EDS analyses) enriched in Al and Na, with significant amounts of K, Ca, P and Cl (Fig. 7EA; Table 2EA).

Chemical profiles across porphyroblastic olivine

The porphyroblastic olivine grains adjacent to areas of Ni mineralisation have variable BSE responses (Figs. 2e, 3a, 3c). X-ray elemental mapping reveals that the margins of porphyroblastic olivine grains in contact with native nickel or

heazlewoodite are significantly enriched in Ni and Fe and depleted in Mg relative to grain cores (Figs. 7, 9EA).

Electron microprobe transects were used to quantify the chemical variation across olivine to native nickel and olivine to heazelwoodite grain boundaries. Porphyroblastic olivine in contact with heazlewoodite displays NiO contents up to 32.7 wt.% at the grain boundary, decreasing to values < 1 wt % at 7-14 μm from the grain boundary (Fig. 8a). The FeO variation is less pronounced than that of NiO, although FeO values increase up to 12.0 wt.%. Porphyroblastic olivine grains adjacent to native nickel (Fig. 8b) are more strongly enriched in FeO (up to 31.8 wt.%) than NiO (up to 5.6 wt.%).

Thermobarometry

Two geothermometers have been used to constrain the equilibration temperature of the spinel harzburgite minerals: i) the Mg-Fe exchange thermometer between porphyroblastic olivine and symplectitic spinel (Ballhaus et al. 1991) and ii) the 'two pyroxenes solvus' thermometer (Bertrand and Mercier 1985; Brey and Koehler 1990), applied to orthopyroxene and clinopyroxene in spinel + pyroxene symplectites. These independent thermometers give consistent results of 664-727°C and 664-717°C, respectively (Table 3EA). Assuming that the sample was in equilibrium with the surrounding mantle, we can infer that these values represent the ambient temperature of the mantle prior to xenolith entrainment. Based on a geothermal gradient of 40-41 mW/m^2, which is considered appropriate for the Kaapvaal craton (e.g. Lazarov et al. 2009), these temperatures correspond to a pressure range of 26-28 kbar (~ 85-90 km). At these conditions the oxygen fugacity of the lithospheric mantle beneath cratons is likely to be between QFM (quartz – fayalite –magnetite buffer) and QFM-1 (Woodland and Koch 2003). We have applied the olivine – orthopyroxene – spinel oxygen barometer of Ballhaus et al. (1991) to better constrain the fO_2 at which sample XM1/422 equilibrated. Although Ballhaus et al. (1991) recommended that this oxygen barometer be restricted to rocks equilibrated at $T \geq 800°C$, we note that temperature has a minimal effect on the calculated fO_2 for sample XM1/422; the calculated fO_2 varies between QFM-1.1 and QFM+1.4 (Table 4EA), for temperature in the range

664-727°C to 800C, with the calculated fO_2 controlled primarily by the Fe^{3+}/Fe_{tot} of symplectitic spinel (0.02-0.10).

Discussion

Petrogenesis of the spinel harzburgite

The texture and mineralogy of harzburgite xenolith XM1/422 indicates that three processes pre-date the Ni mineralisation. Firstly, a partial melting event produced the highly refractory harzburgite protolith ($Mg\#_{Ol}$ = 92.6). At a subsequent stage, the refractory harzburgite is inferred to have experienced silica-rich metasomatism, which produced interstitial grains of orthopyroxene (e.g. Kelemen et al. 1998). The similar composition of the interstitial orthopyroxene and the older porphyroblastic orthopyroxene could be explained if the silica-rich metasomatism occurred long before (0.1-1.0 Gyr?) xenolith entrainment by the host kimberlite, providing time for the orthopyroxene to attain chemical equilibrium. The fine grain size of interstitial orthopyroxene is unlikely to be explained by recrystallisation of porphyroblastic orthopyroxene because, although olivine has more brittle behaviour than orthopyroxene, no fine-grained olivine was observed in the sample. The third event involved breakdown of garnet or Al-Cr-Ca-rich orthopyroxene producing spinel + diopside + orthopyroxene symplectites (Dawson and Smith 1975; Field and Haggerty 1994) during decompression within the mantle.

The Ni mineralisation is constrained as the final event affecting sample XM1/422, because the Ni-rich assemblages are commonly associated with intergrowths of spinel and diopside or orthopyroxene (Fig. 2c, 2d, 2f); and the Ni-rich assemblages include large relict crystals of spinel with compositions varying from similar to that of symplectitic spinel, to compositions enriched in NiO, FeO and (locally) TiO_2 (Table 4, Fig. 6). Inclusions of Ni-Fe-rich clinopyroxene and spinel are common in Ni-Fe-rich olivine (Fig. 3e), suggesting they were inherited from the precursor mineralogy (i.e. the symplectites), and underwent chemical modification. Finally, Ni-rich assemblages partially replace spinel + diopside + orthopyroxene symplectites, but orthopyroxene is almost completely absent and clinopyroxene is not

abundant in the mineralised areas; therefore, it appears that Ni-rich metasomatism caused partial to complete resorption and/or replacement of symplectitic orthopyroxene and, to a lesser extent, diopside.

The occurrence of native nickel and heazlewoodite inclusions in the rims of porphyroblastic olivine (Fig. 4f), and the elevated NiO and FeO contents in porphyroblastic olivine adjacent to native nickel and heazlewoodite (Figs. 7, 8), demonstrate that the Ni mineralisation formed at high temperature in the olivine stability field (i.e. in the mantle).

One possible cause of Ni mineralisation in the mantle is in-situ desulphidation of Fe-Ni monosulphide solid solution (mss) grains, which have been reported in refractory harzburgite xenoliths from several localities (e.g. Alard et al. 2000; Aulbach et al. 2004; Lorand et al. 2004; Lorand and Gregoire 2006). However, this hypothesis is not favoured for xenolith XM1/422 because: i) The mss modal content of refractory harzburgites from the Kaapvaal craton is too low (generally < 0.01 vol%; Lorand and Gregoire 2006) to produce the observed amount of native nickel and sulphides (~ 0.10 vol%); ii) high-T desulphidation of mss produces a residual Fe-rich mss that is not observed in the xenolith, and generates Ni-Cu sulphide melts (Peregoedova et al. 2004) that cannot produce the observed Ni mineralisation (see below); iii) even if mss desulphidation went to completion, mantle mss grains have a lower Ni/Fe ratio (0.1-0.4) than observed in the XM1/422 nickel mineralisation (the Ni/Fe ratio of native nickel and heazlewoodite grains varies between 7 and 350); iv) a process involving sulphur addition, rather than desulphidation, is indicated by the marginal replacement of native nickel grains with heazlewoodite, which likely formed during the latter stages of Ni mineralisation.

Although we cannot completely rule out the possibility that the breakdown of some pre-existing mss produced some of the S and chalcophile elements, the above observations are more easily explained if an externally derived '*Ni-rich metasomatic fluid*' introduced most of the chemical components required for Ni mineralisation. It is suggested that this Ni-rich fluid penetrated into areas occupied by the spinel + pyroxene symplectites, which may have represented zones of local mechanical weakness resulting from a volume increase during decompression.

Composition of Ni-rich fluid(s)

Evidence indicating that the metasomatic fluid (or fluids) was enriched in Ni, Fe, S, Cu, Co, As and Sb (as dissolved ions), and was also Si-bearing, includes: i) the formation of native nickel with variable amounts of Fe and minor Cu and Co, ii) the abundance of heazlewoodite and Ni-Fe-rich olivine, iii) the occurrence of inclusions of Cu-sulphide in heazlewoodite (Fig. 4a) and Ni-Fe-rich relict spinel, and iv) the presence native copper, Ni-Co-rich pentlandite and Sb-bearing gersdorffite in heazlewoodite (Figs. 3d, 4a). The dissolution of pre-existing symplectitic orthopyroxene and diopside would have increased the silica content of the fluid. Alternatively, reactions between the Ni-rich fluid and pyroxenes could have precipitated Ni-Fe-rich olivine, and concentrated Si, Ca, Al and other cations in the residual fluid.

Further constraints on fluid composition are provided by the variation in spinel composition. The spinel grains in the Ni-rich assemblages (i.e. Ni-Fe-rich fine-grained and relict spinel) have high contents of Ni, Fe_{tot}, Fe^{3+} and locally Ti, and low concentrations of Al and Mg, compared to the symplectitic spinel grains (Fig. 6). The excess Al produced by Fe^{3+}-Al^{3+} substitution in the spinel structure (Fig. 6b) was apparently compensated by precipitation of phlogopite and the formation of pockets of Al-rich silicate melt, now preserved as glass inclusions in Ni-Fe-rich relict spinel (Fig. 4e). The crystallisation of Ni-rich phlogopite (locally enriched in Na, Cl and Ti), djerfisherite, F- and Cl-rich apatite, aegirine, and the occurrence of inclusions of silicate glass (enriched in Al, Na, K, Ca, P and Cl), calcite, alkali-carbonate and chlorides in Ni-Fe-rich olivine and spinel (Figs. 4d, 4e), indicates that K, Na, Ti, Ca, P, C (probably as CO_2) and Cl were abundant in the Ni-rich fluid. Calcium and, to a lesser extent, Na were likely provided by dissolution of symplectitic diopside and were scavenged by the fluid from the rims of porphyroblastic olivine. The presence of phlogopite in the Ni-rich assemblages (H_2O ~ 3-4 wt.%; Table 5) suggests that some water was present in the fluid.

In summary the fluid (or fluids) that produced the Ni-rich assemblage appears to have been highly enriched in Ni, Fe (including Fe^{3+}) and volatile elements (S, CO_2, P, Cl, H_2O, As, Sb), with lesser enrichment in Cu, Co, K, Na, Ca and Ti.

It is possible that the Ni-rich assemblages found in XM1/422 and other mantle xenoliths (Lorand and Gregoire 2006), originated from Ni-rich sulphide melts. Indeed, small amounts of sulphide melt with elevated Ni contents can occur in equilibrium with large volumes of peridotite host rock (Barnes et al. 2011). This

sulphide melt could have crystallised Ni-rich sulphides that were then replaced by native nickel following a decrease in sulphur fugacity. However, the replacement of native nickel by heazlewoodite indicates that sulphur was initially undersaturated in the metasomatic fluid, and sulphur fugacity increased, rather than decreasing, with progression of the metasomatic event. In addition, the relatively high concentrations of alkalis, P, Ti, CO_2 and Cl, and the high activity of Fe^{3+} in the metasomatic fluid(s) do not support the involvement of sulphide melts.

Fluid inclusion and petrologic studies of eclogite-facies rocks indicate that 'nominally fluid-immobile elements', such as Ti, Cr and Ni, can be transported by Cl-rich C-O-H fluids (Philippot and Selverstone 1991) at relatively high pressure and temperature (~ 20 kbar and 600°C; Spandler et al. 2011). Experimental investigations provide support for high solubility of transition metal cations, such as Fe^{2+} and Zn^{2+}, in S-Cl-rich C-O-H fluids (e.g. Wood et al. 1987). Therefore, it is likely that the Ni-rich metasomatic agent was a C-O-H fluid, with elevated S and Cl levels enabling transport of dissolved chalcophile metal cations as bisulphide and chloride compounds. Alternatively, an alkali carbonate melt enriched in S, Cl, H_2O could have introduced the inferred inventory of transition metal cations, including Ni.

Temperature - fO_2 - fS_2 conditions and relative timing of Ni mineralisation

The Ni enrichment event resulted in local disequibrium in the host harzburgite xenolith, which is preserved in the μm-scale compositional zoning of the porphyroblastic olivine grains that border native nickel and heazlewoodite (Figs. 2e, 3a, 7). Chemical equilibrium was not achieved in the individual Ni-rich assemblages, as shown by large compositional variations of Ni-Fe-rich olivine, Ni-Fe-rich spinel and Ni-rich phlogopite (Tables 2, 4, 5). The lack of chemical equilibrium hampers a quantitative assessment of the T - fO_2 - fS_2 conditions for the metasomatic event; however, these parameters can be evaluated qualitatively.

Although heazlewoodite itself is a relatively low-T mineral (≤ 565°C; Fleet 2006), its occurrence does not imply a low temperature Ni-rich fluid, because a high-T polymorph of heazlewoodite ($\alpha Ni_{3\pm x}S_2$) crystallises at temperatures up to 862°C (Karup-Moller and Makovicky 1995), and inverts to heazlewoodite at 565°C. The occurrence of native nickel and heazlewoodite suggests that the temperature of formation of the Ni-rich assemblages was lower than 725°C, because native nickel

and the high-T polymorph of heazlewoodite ($\alpha Ni_{3\pm x}S_2$) cannot coexist at higher temperature. Also, the occurrence of heazlewoodite grains with exsolution flames of Ni-Co-rich pentlandite might indicate that the phase $(Ni, Fe, Co)_{3-x}S_2$ was originally produced by the Ni-rich fluid, and then inverted to heazlewoodite + Ni-Co-rich pentlandite. In fact, $(Ni,Fe)_3S_2$ and Co_3S_2 form a complete solid solution above 600°C (Kaneda et al. 1986). Note that grains of $(Ni,Co,Fe)_{3-x}S_2$ with compositions similar to the XM1/422 pentlandite-bearing heazlewoodite, have also been documented as inclusions in olivine and pyroxene xenocrysts from the Lac de Gras kimberlites (Canada; Aulbach et al. 2004).

The relatively low Fe content in the native nickel (< 13.8 wt.%), coupled with the high activity of Fe^{3+} in the fluid(s), indicates crystallisation under oxidising conditions, likely between the Ni-NiO and QFM buffers. The occurrence of native nickel and heazlewoodite supports a low sulphur fugacity close to Ni – Ni_3S_2 equilibrium ($fS_2 \sim 10^{-11}$-10^{-12} at T = 700°C; Table 5EA).

The lack of chemical equilibrium between Ni-rich assemblages and harzburgite minerals can be ascribed to a limited time interval between Ni-rich metasomatism and xenolith entrainment by the kimberlite magma, and relatively low ambient mantle temperatures. To quantify the time interval between Ni-rich metasomatism and xenolith entrainment by the kimberlite magma, we have estimated the time required for Ni to diffuse into a porphyroblastic olivine grain adjacent to native nickel and heazlewoodite, using the formulation of Chakraborty (2010; see Appendix 1). If diffusion occurred at high temperature (~ 1000°C), the time required for the observed Ni diffusion into olivine would be less than a few hundred years. Whereas, if diffusion operated at temperatures equivalent to the equilibrium conditions of the xenolith minerals (~ 700°C), Ni diffusion would require up to 10 Myr (depending on oxygen fugacity and crystallographic orientation), but more likely within ca.2 Myr (assuming diffusion along the 'fastest' *c* axis (Chakraborty 2010) and fO_2 = QFM). If diffusion occurred at temperatures lower than the harzburgite equilibration (≤ 650°C), i.e. after xenolith emplacement in the crust, modelling of diffusion duration would yield unrealistic diffusion times longer than the age of kimberlite emplacement (84 Myr): this is a definitive evidence that the metasomatic event occurred in the mantle at temperatures at least above 650°C. The fine grain-size of the granoblastic Ni-Fe-rich olivine grains suggests that the metasomatic fluid temperature decreased rapidly towards ambient mantle conditions during reaction

with the symplectite minerals. Therefore, it is suggested that diffusion of Ni into porphyroblastic olivine was controlled by the ambient temperature of the mantle and may have continued for ca.2 Myr. The relatively coarse size (up to 200 μm) of native nickel grains and the presence of re-crystallised porphyroblastic olivine with inclusions of native nickel and heazlewoodite, is consistent with residence in the shallow mantle for a short period of time (≤ 2 Myr) prior to kimberlite eruption. The emplacement of kimberlite magmas into the upper crust is considered to take place through multiple pulses on a Myr time-scale, because some of the main kimberlite fields display age ranges of up to 10 Myr (Gregoire et al. 2006; Mitchell 1986). Therefore, it is proposed that Ni metasomatism may be broadly related to kimberlite magmatism in the Kimberley area. Moreover, kimberlites occur in every known craton and surrounding regions (Mitchell 1986), and kimberlite magmas have been emplaced in the upper crust since at least 1.8 Gyr (Donnelly et al. 2011). Therefore, kimberlite-related metasomatism has affected large sectors of craton and off-craton regions for a large part of the Earth history, and consequently, the effects of kimberlite-related metasomatism should not be considered local or of short duration.

In conclusion, infiltration of small volumes of C-O-H fluids (or alkali carbonate melts) with variable composition is the preferred hypothesis to explain the chemical disequilibrium preserved in the Ni-rich assemblages of xenolith XM1/422. In addition, the grain boundary alteration of some spinel + pyroxenes symplectites to phlogopite and Ni-poor spinel grains that hosts inclusions of phases enriched in alkalis, Ca, CO_2, P and Cl (Figs. 2b, 2EA, 3EA), suggests that the rock was also permeated by a Ni-poor alkali-rich C-O-H fluid(s) (or alkali carbonate melts), which likely postdated the Ni-rich fluid(s).

Origin of the Ni-rich metasomatic fluid

The metasomatic fluid involved in the Ni mineralisation likely acquired Ni and Fe through the breakdown of mantle minerals enriched in these elements. Sulphides are the only phases that host abundant Ni and Cu, as well as S, Co and Fe, in the Earth's mantle. Therefore, breakdown of sulphides (probably mss) is likely to have contributed Ni, Fe and S, and lesser Cu and Co to the metasomatic fluid. This breakdown could have occurred either in the source region of the fluid, during its ascent in the mantle, or where the Ni mineralisation formed. However, as in-situ

desulphidation of mss could not have produced the bulk Ni mineralisation, mss breakdown was not the only Ni source. Interaction of the fluid with refractory lithospheric mantle material during fluid migration likely scavenged Ni, Co and possibly Cu from other more abundant mineral phases such as orthopyroxene and olivine. The depletion in Ni and Co observed in the rims of porphyroblastic orthopyroxene (Table 3) in xenolith XM1/422, implies that Ni and Co, which are incompatible in orthopyroxene, were scavenged by the percolating metasomatic fluid(s), as per the chromatographic column model (Navon and Stolper 1987). Alternatively, if the original fluid was enriched in silica, it could react with olivine to form metasomatic orthopyroxene, which contains less NiO, FeO (Ishimaru and Arai 2008; Kelemen et al. 1998) and Co (Gregoire et al. 2000) than olivine, thus liberating Ni, Fe and Co into the residual fluid phase, while depleting it in silica.

The primary source of the metasomatic fluid remains elusive. The initial fluid could have derived from differentiation of ascending batches of proto-kimberlite magma. This fluid would have been rich in volatile and incompatible elements, with elevated concentrations of Ni, Fe and other chalcophile element achieved by sulphide breakdown and/or interaction with silicate minerals of the refractory mantle. Alternatively, the thermal anomaly associated with ascending proto-kimberlite magmas could have caused partial melting in areas of the lithospheric mantle affected by older episodes of metasomatic enrichment. The melts produced by partial melting of the metasomatised lithospheric mantle would have been enriched in alkalis and volatile components (e.g. Litasov et al. 2010; Wallace and Green 1988; Wyllie and Zhang 1975), and locally in Ni, Fe, Cu, Co and S if sulphides occurred in the source region. During migration through the mantle, these melts would have undergone differentiation, interaction with surrounding rocks and, ultimately, evolution to the metal-rich C-O-H fluids (or alkali carbonate melts) that enriched sample XM1/422.

However, we note that: i) The occurrence of native nickel and other native metals and alloys in mantle rocks is easily overlooked because their recognition requires detailed observations by SEM [or reflected light microscopy if the alloys are sufficiently large (> 10-20 μm)]; ii) metasomatic fluids with elevated contents of Cu, Ni, PGEs, alkalis and volatiles also occur in domains of the lithospheric mantle, including orogenic peridotitic massifs and the sub-oceanic lithospheric mantle, which were not affected by kimberlite magmatism (Alard et al. 2011; Fiorentini and Beresford 2008; Garuti et al. 1997 and 2001; Lorand and Alard 2001; Lorand et al.

2004). This suggests that metal enrichment by metasomatism could be widespread in the lithospheric mantle, and might be associated with any thermal anomaly that produces a C-O-H fluid or a low-degree partial melt. Therefore, Ni-rich metasomatism may not be intrinsically linked to kimberlite genesis, despite the association in the current study.

Conclusions

We have documented the occurrence of Ni mineralisation in a refractory spinel harzburgite xenolith from the lithospheric mantle sampled by the Bultfontein kimberlite (Kimberley, South Africa). The Ni mineralisation includes relatively large grains of native nickel, heazlewoodite and minor djerfisherite, and fine-grained granoblastic domains of Ni-Fe-rich olivine (up to 37.5 wt.% NiO) with heazlewoodite, Ni-Fe-rich spinel, Ni-Fe-rich clinopyroxene, Ni-rich phlogopite (up to 22.4 wt.% NiO), and minor apatite and aegirine. Calcite, alkali-carbonates and chlorides are preserved as inclusions within the Ni-rich minerals. The Ni mineralisation observed in xenolith XM1/422, and in other mantle xenoliths from the Kimberley area, was likely produced by C-O-H fluid(s) (or carbonate melts) enriched in transition metal cations (Ni, Fe, Cu, Co), alkalis, S, Cl, As and Sb. The Ni mineralisation preferentially deposited in the areas occupied by the spinel + pyroxene symplectites and partially overprinted the pre-existing phases. We propose that sulphide breakdown and fluid reaction with refractory mantle rocks contributed to the fluid's enrichment in Ni and other metallic cations. Although the ultimate source of the metasomatic fluid remains elusive, the preservation of chemical disequilibrium in the Ni-rich assemblages, coupled with modelling of Ni diffusion into porphyroblastic olivine grains, suggests that the metasomatic event was related to kimberlite magmatism in the Kimberley area. Our study suggests that alkali-S-Cl-rich C-O-H fluids can mobilise Ni, Cu, Co and probably other metallic cations of economic importance.

Acknowledgements We thank Chris Ballhaus for constructive discussions at the early stage of this study and for editorial handling; Fanus Viljoen, Michel Gregoire and Jean-Pierre Lorand for

constructive reviews; Reid Keays, Sonja Aulbach and Antje Wildau for useful discussions during manuscript preparation; Alan Greig for help with LA-ICP-MS analyses, and Graham Hutchinson for support with the SEM imaging and EMP analyses at the University of Melbourne. Finally, we acknowledge De Beers Consolidated Mines Ltd. for providing DP with the sample for this study. AG's PhD research is supported by an International Australian Postgraduate Award, the 2011 John Hodgson Scholarship, and the 2012 AusIMM Bicentennial Gold Endowment.

Appendix 1. Model of diffusion duration of Ni into olivine

The Ni diffusion profiles in porphyroblastic olivine can be modelled by applying Fick's second law to estimate the duration of the diffusion process. The diffusion coefficient for Ni in olivine has been determined at different values of temperature, pressure and oxygen fugacity using the formulation of Chakraborty (2010). Note that in the olivine lattice, diffusion operates 6 times faster along the *c* axis than along the other two crystallographic axes (Chakraborty 2010, and references therein). For this calculation we have assumed temperatures equivalent to, or higher than, the equilibration temperature of the xenolith minerals (664-727°C). Pressure has a negligible effect on the value of the diffusion coefficient. The oxygen fugacity is assumed to have been intermediate between the QFM buffer (which is the maximum value previously calculated for the shallow spinel facies mantle beneath the Kaapvaal craton; Woodland and Koch 2003), and the Ni-NiO buffer (which is indicated by the crystallisation of nearly pure native nickel; Carmichael 1991). The Ni chemical profiles in olivine adjacent to heazlewoodite show Ni diffusion at distances between 73 and 85 μm; consequently we have modelled Ni diffusion into olivine up to a length scale of 80 μm. Based on the above input parameters, and considering diffusion along the 'fastest' axis *c*, Ni could diffuse 80 μm into olivine over a minimum period of ca. 100 yr at 1000 ºC, or over a maximum period of 0.7 - 1.7 Myr at 700 ºC (see Online Resource Table 6EA).

References

Alard O, Griffin WL, Lorand JP, Jackson SE, O'Reilly SY (2000) Non-chondritic distribution of the highly siderophile elements in mantle sulphides. Nature 407:891-894

Alard O, Lorand J-P, Reisberg L, Bodinier J-L, Dautria J-M, O'Reilly SY (2011) Volatile-rich Metasomatism in Montferrier Xenoliths (Southern France): Implications for the Abundances of Chalcophile and Highly Siderophile Elements in the Subcontinental Mantle. J Petrol 52:2009-2045

Allsopp HL, Barrett DR (1975) Rb-Sr determinations on South african kimberlite pipes. Phys Chem Earth 9:615-617

Andersen T, O'Reilly SY, Griffin WL (1984) The trapped fluid phase in upper mantle xenoliths from Victoria, Australia: implications for mantle metasomatism. Contrib Mineral Petrol 88:72-85

Aulbach S, Griffin WL, Pearson NJ, O'Reilly SY, Kivi K, Doyle BJ (2004) Mantle formation and evolution, Slave Craton: constraints from HSE abundances and Re-Os isotope systematics of sulfide inclusions in mantle xenocrysts. Chem Geol 208:61-88

Ballhaus C, Berry R, Green D (1991) High pressure experimental calibration of the olivine-orthopyroxene-spinel oxygen geobarometer: implications for the oxidation state of the upper mantle. Contrib Mineral Petrol 107:27-40

Barnes SJ, Godel BM, Locmelis M, Fiorentini ML, Ryan CG (2011) Extremely Ni-rich Fe-Ni sulfide assemblages in komatiitic dunite at Betheno, Western Australia: results from synchrotron X-ray fluorescence mapping. Austral J Earth Sci 58:691-709

Bertrand P, Mercier J-CC (1985) The mutual solubility of coexisting ortho- and clinopyroxene: toward an absolute geothermometer for the natural system? Earth Planet Sci Lett 76:109-122

627 Burgess SR, Harte B (2004) Tracing Lithosphere Evolution through the Analysis of Heterogeneous
628 G9-G10 Garnets in Peridotite Xenoliths, II: REE Chemistry. J Petrol 45:609-633
629 Carmichael ISE (1991) The redox states of basic and silicic magmas: a reflection of their source
630 regions? Contrib Mineral Petrol 106:129-141
631 Chakraborty S (2010) Diffusion Coefficients in Olivine, Wadsleyite and Ringwoodite. Rev Mineral
632 Geochem 72:603-639
633 Dawson JB, Smith JV (1975) Chromite-silicate intergrowths in upper-mantle peridotites. Phys Chem
634 Earth 9:339-350
635 de Waal SA, Calk LC (1973) Nickel Minerals from Barberton, South Africa: VI. Liebenbergite, a
636 Nickel Olivine. Am Mineral 58:733-735
637 Donnelly C, Griffin W, O'Reilly S, Pearson N, Shee S (2011) The Kimberlites and related rocks of the
638 Kuruman Kimberlite Province, Kaapvaal Craton, South Africa. Contrib Mineral Petrol
639 161:351-371
640 Field SW, Haggerty SE (1994) Symplectites in upper mantle peridotites: Development and
641 implications for the growth of subsolidus garnet, pyroxene and spinel. Contrib Mineral Petrol
642 118:138-156
643 Fiorentini ML, Beresford SW (2008) Role of volatiles and metasomatized subcontinental lithospheric
644 mantle in the genesis of magmatic Ni–Cu–PGE mineralization: insights from in situ H, Li, B
645 analyses of hydromagmatic phases from the Valmaggia ultramafic pipe, Ivrea-Verbano Zone
646 (NW Italy). Terra Nova 20:333-340
647 Fleet ME (2006) Phase equilibria at high temperatures. Rev Mineral Geochem 61:365-419
648 Fleet ME, Wu T-W (1995) Volatile transport of precious metals at 1000°C: Speciation, fractionation,
649 and effect of base-metal sulfide. Geochimi Cosmochim Acta 59:487-495
650 Frezzotti ML, Ferrando S, Peccerillo A, Petrelli M, Tecce F, Perucchi A (2010) Chlorine-rich
651 metasomatic H_2O-CO_2 fluids in amphibole-bearing peridotites from Injibara (Lake Tana
652 region, Ethiopian plateau): Nature and evolution of volatiles in the mantle of a region of
653 continental flood basalts. Geochim Cosmochim Acta 74:3023-3039
654 Gaetani GA, Grove TL (1999) Wetting of mantle olivine by sulfide melt: implications for Re/Os ratios
655 in mantle peridotite and late-stage core formation. Earth Planet Sci Lett 169:147-163
656 Garuti G, Oddone M, Torres-Ruiz J (1997) Platinum-group-element distribution in subcontinental
657 mantle: evidence from the Ivrea Zone (Italy) and the Betic - Rifean cordillera (Spain and
658 Morocco). Canad J Earth Sci 34:444-463
659 Garuti G, Bea F, Zaccarini F, Montero P (2001) Age, Geochemistry and Petrogenesis of the Ultramafic
660 Pipes in the Ivrea Zone, NW Italy. J Petrol 42:433-457
661 Giuliani A, Kamenetsky VS, Phillips D, Kendrick MA, Wyatt BA, Goemann K (2012) The nature of
662 alkali-carbonate fluids in the sub-continental lithospheric mantle. Geology, in press, doi
663 10.1130/G33221.1
664 Gregoire M, Moine BN, O'Reilly SY, Cottin JY, Giret A (2000) Trace Element Residence and
665 Partitioning in Mantle Xenoliths Metasomatized by Highly Alkaline, Silicate- and Carbonate-
666 rich Melts (Kerguelen Islands, Indian Ocean). J Petrol 41:477-509
667 Gregoire M, Rabinowicz M, Janse AJA (2006) Mantle Mush Compaction: a Key to Understand the
668 Mechanisms of Concentration of Kimberlite Melts and Initiation of Swarms of Kimberlite
669 Dykes. J Petrol 47:631-646
670 Harte B (1987) Metasomatic events recorded in mantle xenoliths: An overview. In: Nixon PH (ed)
671 Mantle xenoliths. John Wiley & Sons, New York, pp 625-640
672 Harte B (2012) Mineral associations in diamonds from the lowermost upper mantle and uppermost
673 lower mantle. 10th Internat Kimb Confer, Bangalore, India, Ext abstr n.190
674 Ishimaru S, Arai S (2008) Nickel enrichment in mantle olivine beneath a volcanic front. Contrib
675 Mineral Petrol 156:119-131
676 Ishimaru S, Arai S, Shukuno H (2009) Metal-saturated peridotite in the mantle wedge inferred from
677 metal-bearing peridotite xenoliths from Avacha volcano, Kamchatka. Earth Planet Sci Lett
678 284:352-360
679 Jacob DE, Kronz A, Viljoen KS (2004) Cohenite, native iron and troilite inclusions in garnets from
680 polycrystalline diamond aggregates. Contrib Mineral Petrol 146:566-576
681 Jochum KP, Stoll B (2008) Reference materials for elemental and isotopic analyses by LA–(MC)–ICP–
682 MS: successes and outstanding needs. In: Sylvester P (ed) Laser Ablation ICP–MS in the
683 Earth Sciences: Current Practices and Outstanding Issues, Mineral Assoc Canada, pp 147-168
684 Kaneda H, Takenouchi S, Shoji T (1986) Stability of pentlandite in the Fe-Ni-Co-S system. Mineral
685 Depos 21:169-180

686 Karup-Moller S, Makovicky E (1995) The phase system Fe-Ni-S at 725°C. Neue Jaharb Mineral
687 Mhon:1-10
688 Keays RR, Sewell DKB, Mitchell RH (1981) Platinum and palladium minerals in upper mantle-derived
689 lherzolites. Nature 294:646-648
690 Kelemen PB, Hart SR, Bernstein S (1998) Silica enrichment in the continental upper mantle via
691 melt/rock reaction. Earth Planet Sci Lett 164:387-406
692 Kinny PD, Dawson JB (1992) A mantle metasomatic injection event linked to late Cretaceous
693 kimberlite magmatism. Nature 360:726-728
694 Lazarov M, Woodland AB, Brey GP (2009) Thermal state and redox conditions of the Kaapvaal
695 mantle: A study of xenoliths from the Finsch mine, South Africa. Lithos 112S:913-923
696 Litasov KD, Safonov OG, Ohtani E (2010) Origin of Cl-bearing silica-rich melt inclusions in
697 diamonds: Experimental evidence for an eclogite connection. Geology 38:1131-1134
698 Lorand J-P, Alard O (2001) Platinum-group element abundances in the upper mantle: new constraints
699 from in situ and whole-rock analyses of Massif Central xenoliths (France). Geochim
700 Cosmochim Acta 65:2789-2806
701 Lorand J-P, Alard O, Luguet A (2010) Platinum-group element micronuggets and refertilization
702 process in Lherz orogenic peridotite (northeastern Pyrenees, France). Earth Planet Sci Lett
703 289:298-310
704 Lorand J-P, Delpech G, Gregoire M, Moine B, O'Reilly SY, Cottin J-Y (2004) Platinum-group
705 elements and the multistage metasomatic history of Kerguelen lithospheric mantle (South
706 Indian Ocean). Chem Geol 208:195-215
707 Lorand J-P, Gregoire M (2006) Petrogenesis of base metal sulphide assemblages of some peridotites
708 from the Kaapvaal craton (South Africa). Contrib Mineral Petrol 151:521-538
709 Lorand J-P, Keays RR, Bodinier JL (1993) Copper and Noble Metal Enrichments Across the
710 Lithosphere-Asthenosphere Boundary of Mantle Diapirs: Evidence from the Lanzo Lherzolite
711 Massif. J Petrol 34:1111-1140
712 Luguet A, Shirey SB, Lorand J-P, Horan MF, Carlson RW (2007) Residual platinum-group minerals
713 from highly depleted harzburgites of the Lherz massif (France) and their role in HSE
714 fractionation of the mantle. Geochim Cosmochim Acta 71:3082-3097
715 Mitchell RH (1986) Kimberlites: Mineralogy, Geochemistry and Petrology. Plenum Publishing
716 Company, New York, pp 442
717 Mungall JE, Su S (2005) Interfacial tension between magmatic sulfide and silicate liquids: Constraints
718 on kinetics of sulfide liquation and sulfide migration through silicate rocks. Earth Planet Sci
719 Lett 234:135-149
720 Navon O, Stolper E (1987) Geochemical Consequences of Melt Percolation: The Upper Mantle as a
721 Chromatographic Column. J Geol 95:285-307
722 Pearson DG, Canil D, Shirey SB (2003) Mantle Samples Included in Volcanic Rocks: Xenoliths and
723 Diamonds. In: Carlson R (ed) Treatise on Geochemistry, Vol.2, The Mantle and Core.
724 Pergamon, Oxford, pp 171-275
725 Peregoedova A, Barnes S-J, Baker DR (2004) The formation of Pt-Ir alloys and Cu-Pd-rich sulfide
726 melts by partial desulfurization of Fe-Ni-Cu sulfides: results of experiments and implications
727 for natural systems. Chem Geol 208:247-264
728 Philippot P, Selverstone J (1991) Trace-element-rich brines in eclogitic veins: implications for fluid
729 composition and transport during subduction. Contrib Mineral Petrol 106:417-430
730 Rose LA, Brenan JM (2001) Wetting Properties of Fe-Ni-Co-Cu-O-S Melts against
731 Olivine:Implications for Sulfide Melt Mobility. Econ Geol 96:145-157
732 Sharygin VV, Golovin AV, Pokhilenko NP, Kamenetsky VS (2007) Djerfisherite in the Udachnaya-
733 East pipe kimberlites (Sakha-Yakutia, Russia): paragenesis, composition and origin. Eu J
734 Mineral 19:51-63
735 Smith CB (1983) Pb, Sr and Nd isotopic evidence for sources of southern African Cretaceous
736 kimberlites. Nature 304:51-54
737 Spandler C, Pettke T, Rubatto D (2011) Internal and External Fluid Sources for Eclogite-facies Veins
738 in the Monviso Meta-ophiolite, Western Alps: Implications for Fluid Flow in Subduction
739 Zones. J Petrol 52:1207-1236
740 Wallace ME, Green DH (1988) An experimental determination of primary carbonatite magma
741 composition. Nature 335:343-346
742 Wood SA, Crerar DA, Borcsik MP (1987) Solubility of the assemblage pyrite-pyrrhotite-magnetite-
743 sphalerite-galena-gold-stibnite-bismuthinite-argentite-molybdenite in H_2O-NaCl-CO_2
744 solutions from 200 to 350°C. Econ Geol 82:1864-1887

745 Woodhead JD, Hellstrom J, Hergt JM, Greig A, Maas R (2007) Isotopic and Elemental Imaging of
746 Geological Materials by Laser Ablation Inductively Coupled Plasma-Mass Spectrometry.
747 Geostand Geoanal Res 31:331-343
748 Woodland AB, Koch M (2003) Variation in oxygen fugacity with depth in the upper mantle beneath
749 the Kaapvaal craton, Southern Africa. Earth Planet Sci Lett 214:295-310
750 Wyllie PJ, Huang W-L (1975) Peridotite, kimberlite, and carbonatite explained in the system CaO-
751 MgO-SiO_2-CO_2. Geology 3:621-624
752 Yaxley GM, Green DH, Kamenetsky VS (1998) Carbonatite Metasomatism in the Southeastern
753 Australian Lithosphere. J Petrol 39:1917-1930
754

Figure captions.

Fig 1 Scanned image of XM1/422 thin section, showing the granular texture of the rock. The small brown areas are the sites of spinel + pyroxenes symplectites (Spl+Px)

Fig. 2 SEM (a,c-f) and FE-SEM (b) back-scattered electron (BSE) images of spinel + pyroxene symplectites and Ni mineralisation in xenolith XM1/422. **a** Spinel (Spl) + diopside (Dps) + orthopyroxene (Opx) symplectite; **b** spinel + diopside symplectite with margins altered to phlogopite (Phl). Spinel grains host abundant inclusions and show variable BSE response (see Online Resource Fig. 3EA); **c, d, e, f** symplectites replaced to different degrees by Ni-rich minerals such as native nickel (Ni), heazlewoodite (Hz) and Ni-Fe-rich olivine (Ni-Ol); In **e,** note the BSE zoning in porphyroblastic olivine (Ol) adjacent to heazlewoodite. (Srp: serpentine)

Fig. 3 SEM BSE (**a**), FE-SEM BSE (**b**,**c**,**d**) and FE-SEM secondary electron (SE; **e**,**f**) images of granoblastic Ni-Fe-rich olivine (Ni-Ol) domains. In **a** and **c,** note the variation in BSE response for porphyroblastic olivine (Ol) adjacent to the mineralised areas; **d** ×3000 view of Sb-bearing gersdorffite (Grs; [NiAsS)] inclusions in heazlewoodite (Hz); **e** inclusions of Ni-Fe-rich spinel (Ni-Spl) in Ni-Fe-rich olivine; **f** inclusions of Ni-Fe-rich spinel in Ni-rich phlogopite (Ni-Phl) that is interstitial to Ni-Fe-rich olivine

Fig. 4 FE-SEM BSE images of minerals in the Ni-rich assemblages. **a** Inclusions of native copper (Cu), Cu-sulphide (CuS), and Ni-Co-rich pentlandite (Ni-Co Pn) in heazlewoodite (Hz); **b** and **d** Ni-Fe-Ti-rich spinel (Spl) rim on symplectitic spinel (Spl core) with inclusions of Cu and Ni sulphides, alkali-carbonates (Akc), apatite, calcite and chlorides (not shown); **c** intergrowth of Ni-Fe-rich relict spinel and heazlewoodite with minor phlogopite (Ni-Phl); **e** re-crystallised Ni-Fe-rich relict spinel with inclusions of silicate glass displaying negative crystal shapes of the spinel host (see Fig.6EA for EDS spectra, and Table 2EA for chemical composition); **f** inclusion of native nickel with small heazlewoodite apophyses (not shown) in the rim of porphyroblastic olivine (Ol). (Srp: serpentine)

Fig. 5 Ternary plot showing the molecular proportions of forsterite (Fo: $MgSiO_4$), fayalite (Fa: $FeSiO_4$), and liebenbergite (Lie: $NiSiO_4$) in fine-grained, Ni-Fe-rich olivine and coarse-grained, porphyroblastic olivine

Fig. 6 a NiO *vs* atomic Fe^{3+}/Fe_{tot} and **b** Al_2O_3 *vs* Fe_2O_3 plots for spinel grains in xenolith XM1/422. In legend 'Ni-Fe-rich' refers to Ni-Fe-rich fine-grained spinel crystals. See Table 1 for textural occurrence of each spinel type

Fig. 7 SEM BSE image and EDS x-ray elemental maps of native nickel (Ni), heazlewoodite (Hz) and the surrounding coarse grains of porphyroblastic olivine (Ol). Note that the variation in the BSE response in porphyroblastic olivine grains corresponds to an increase in the concentrations of Fe and Ni (not evident), and a concomitant decrease in Mg

Fig. 8. Examples of chemical profiles across porphyroblastic olivine grains in contact with heazlewoodite (**a**) and native nickel (**b**). The positions of these and other profiles are reported in the Online Resource Fig. 8EA

Tables

Table 1. Summary of textural and chemical features of silicate and oxide minerals in xenolith XM1/422

mineral type	*denomination*	*occurrence*	*texture*	*composition*
olivine	porphyroblastic	harzburgite	coarse-grained	high Fo
	Ni-Fe-rich	Ni-rich mineralisation	fine-grained	NiO-FeO rich
orthopyroxene	porphyroblastic	harzburgite	coarse-grained	high En
	interstitial	harzburgite	interstitial	high En
	symplectitic	symplectites	intergrown with Spl+Cpx	CaO poor
clinopyroxene	diopside	symplectites	intergrown with Spl±Opx	NiO-FeO poor
	Ni-Fe-rich	Ni-rich mineralisation	mainly as inclusions	NiO-FeO rich
spinel	symplectitic	symplectites	intergrown with Cpx±Opx	NiO-Fe_2O_3 poor
	altered Ni-poor	altered margins of symplectites	enriched in inclusions	NiO poor
	relict	Ni-rich mineralisation	relatively large	variable
	Ni-Fe-rich fine-grained	Ni-rich mineralisation	fine-grained and as inclusions	NiO-FeO_{tot} rich
phlogopite	Ni-poor	altered margins of symplectites	fine-grained	NiO-poor
	Ni-rich	Ni-rich mineralisation	fine-grained	NiO-FeO rich

Spl spinel; Cpx clinopyroxene; Opx orthopyroxene; Fo fosterite; En enstatite

Table 2. Average and representative major oxide data (wt%) for olivine, orthopyroxene and clinopyroxene in xenolith XM1/422

occurr.	*porphyroblastic*							*symplectitic*			*Ni-rich mineralisation*			
mineral type	*Ol*		*Opx core*		*Opx rim*	*Opx interstitial*		*Opx*		*diopside*	*Ni-Fe-rich Ol*	*Ni-Fe-rich Ol*	*Ni-Fe-rich Cpx*	*aegirine*
label	average[a]	1σ	average[b]	1σ	422Opx-29	average[c]	1σ	average[c]	1σ	422-Cpx2	Ol 7/5	Ol3-21-1	422 CpxNi	422-Aeg2
SiO_2	41.08	0.28	56.14	0.12	56.14	55.99	0.13	56.40	0.19	53.81	35.02	35.02	52.60	51.90
TiO_2	0.01	0.01	0.01	0.00	bdl	0.01	0.01	bdl		0.02	nd	nd	bdl	0.01
Al_2O_3	bdl		2.86	0.08	2.57	2.99	0.06	2.38	0.18	1.79	nd	nd	1.90	0.15
Cr_2O_3	0.01	0.01	0.91	0.05	0.83	0.88	0.02	0.85	0.09	1.16	nd	0.07	2.38	0.02
FeO	7.13	0.10	4.46	0.07	4.75	4.46	0.08	4.74	0.09	1.39	7.41	20.11	7.22	30.01
MnO	0.11	0.02	0.11	0.01	0.11	0.11	0.01	0.12	0.03	0.03	0.09	0.10	0.07	0.05
MgO	51.81	0.20	34.90	0.11	35.43	34.85	0.15	35.52	0.41	17.64	20.55	28.94	12.45	0.86
NiO	0.37	0.02	0.10	0.04	0.06	0.07	0.03	0.06	0.03	bdl	37.45	14.98	3.10	1.87
CaO	0.01	0.01	0.72	0.03	0.58	0.73	0.03	0.48	0.08	23.96	nd	0.03	17.72	0.91
Na_2O	nd		0.02	0.01	0.02	0.02	0.02	0.02	0.01	0.59	nd	nd	2.18	12.40
Total	100.53		100.24		100.49	100.10		100.58		100.39	100.52	99.24	99.63	98.20
Mg#	92.57	0.10	93.18	0.09	92.93	93.22	0.09	92.96	0.06	95.84	45.76	59.92	68.51	9.48

[a] 22 analyses; [b] 10 analyses; [c] 4 analyses; nd not determined; bdl below detection limit; Mg# = 100×Mg/(Mg+Fe+Ni)
Ol olivine; Cpx clinopyroxene; Opx orthopyroxene

Table 3. Average trace element contents (ppm) of porphyroblastic olivine and orthopyroxene

	Ol core		*Ol rim*		*Opx core*		*Opx rim*	
	average[a]	1σ	average[a]	1σ	average[b]	1σ	average[c]	1σ
Li	0.43	0.05	0.48	0.08	2.59	0.75	0.80	0.26
Na	2.24	0.46	1.70	0.81	165	4.94	173	12.65
Ca	83	10	44	11	4632	147	4605	262
Ti	7.3	0.6	7.6	0.5	15.4	5.1	15.4	4.2
Cr	38	7	20	6	5629	219	5254	503
Co	125	1	123	4	51	1	47	1
Ni	2789	49	2782	45	640	24	525	27
Zn	34.4	1.2	31.1	4.7	29.4	0.2	28.2	0.9
Mo	0.07	0.01	0.07	0.02	0.07	0.13	0.03	0.05
Cu	0.02	0.01	0.02	0.02	0.08	0.09	0.09	0.12
Sc	nd		nd		18.2	0.4	18.5	0.7
V	nd		nd		69	3	80	6

[a] 8 analyses; [b] 10 analyses; [c] 11 analyses; nd not determined; Ol olivine; Opx orthopyroxene

Table 4. Average and representative major oxide data (wt%) for spinel in xenolith XM1/422

spinel type	*symplectitic*		*altered Ni-poor*		*enriched relict*	*enriched relict*	*enriched relict*	*Ni-Fe-rich fine-grain*
label	average[b]	1σ	average[c]	1σ	422-Spl-10	422Splnrim	422 Spl c-b	422 Ni-Spl
SiO_2	0.03	0.01	0.06	0.05	bdl	0.06	0.15	bdl
TiO_2	0.01	0.01	0.04	0.03	0.01	6.67	bdl	bdl
Al_2O_3	23.30	0.97	19.85	1.37	22.31	6.18	13.56	17.15
Cr_2O_3	46.86	0.81	49.58	0.53	46.23	42.73	44.55	45.66
FeO	15.99	0.54	14.21	0.59	21.36	28.17	30.57	25.56
MnO	0.17	0.02	0.21	0.03	0.13	0.32	0.16	0.09
MgO	13.47	0.58	14.21	0.34	9.42	11.89	7.22	4.72
ZnO	nd		0.26	0.10	0.48	nd	nd	nd
NiO	0.04	0.02	0.11	0.08	0.53	1.67	2.02	5.72
V_2O_3	0.16	0.05	0.25	0.03	0.17	0.19	0.16	0.15
Total	100.09		98.75		100.64	97.87	98.38	99.05
Fe_2O_3[a]	1.10	0.56	1.58	0.46	0.83	10.74	10.74	4.32
FeO rec	15.00	0.86	12.80	0.18	20.61	18.51	20.91	21.67
Total rec	100.13	0.36	98.65	0.51	100.24	98.95	99.46	99.48
$Cr/(Fe^{3+}+Cr+Al)$	0.57	0.01	0.63	0.02	0.58	0.69	0.69	0.61
Mg#	61.5	0.02	66.4	0.01	44.9	51.3	38.1	22.5
Fe^{3+}/Fe_{tot}	0.06	0.03	0.11	0.02	0.05	0.34	0.32	0.13

[a] Fe^{3+} calculated by stoichiometry; [b] 5 analyses; [c] 3 analyses; bdl below detection limit; nd not determined

Mg# = $100 \times Mg/(Mg+Fe^{2+}+Ni)$

Table 5. Representative major element data (wt%) for phlogopite in xenolith XM1/422

occurrence	*altered symplectites*		*Ni-rich mineralisation*		
type	*Ni-poor*			*Ni-rich*	
label	422Phl3-14	422Phl4-15	422-NiPhl	422-NiPhl3	422 Phl n2
SiO_2	40.53	41.50	35.27	34.07	38.02
TiO_2	1.05	0.16	0.00	0.02	1.74
Al_2O_3	12.01	11.81	14.55	13.77	13.84
Cr_2O_3	1.42	1.19	1.28	1.24	1.94
FeO	2.94	2.98	6.94	6.21	4.12
MnO	0.02	0.0	0.01	0.06	0.00
MgO	25.69	26.77	11.26	8.37	22.79
NiO	0.26	0.27	16.58	22.42	1.86
CaO	bdl	bdl	bdl	bdl	0.03
Na_2O	0.59	0.94	1.02	0.95	0.29
K_2O	9.67	9.02	7.87	7.17	9.87
F	0.68	0.79	nd[b]	nd[b]	nd[b]
Cl	0.02	0.01	0.31	0.37	0.02
Total	94.90	95.46	95.10	94.65	94.51
H_2O rec.[a]	3.85	3.84	3.73	3.59	4.11
Subtotal	98.75	99.30	98.83	98.24	98.62
O=F,Cl	0.29	0.34	0.07	0.08	0.00
Total	98.46	98.97	98.76	98.16	98.62

[a] H_2O calculated by stoichiometry; nd not determined; bdl below detection limit
[b] F was not determined in Ni-rich phlogopite as preliminary EDS analyses never show the F peak

Table 6. Representative major element data (wt%) of native nickel and heazlewoodite in xenolith XM1/422

mineral	*native nickel*					*heazlewoodite*	
label	422 Ni	422 Ni4 2	422t-Ni1s	422t-Ni2	422t-Ni3	422-NiS-7	422-NiS[a]
Fe	2.03	10.82	1.25	13.82	4.06	0.21	3.13
Co	0.22	0.50	0.05	0.36	0.25	0.04	0.16
Ni	97.40	88.93	97.28	84.11	94.27	73.14	72.30
Cu	0.54	bdl	0.64	0.57	0.67	0.16	bdl
Zn	bdl	bdl	nd	nd	nd	0.09	bdl
S	0.02	0.02	0.03	0.01	0.02	26.99	22.12
Total	100.21	100.26	99.24	98.87	99.27	100.63	97.71
atomic %							
Fe	2.13	11.28	1.32	14.59	4.29	0.18	2.83
Co	0.22	0.50	0.05	0.36	0.25	0.04	0.14
Ni	97.12	88.20	97.98	84.50	94.80	59.45	62.21
Cu	0.50	0.00	0.59	0.53	0.62	0.12	0.00
Zn	0.00	0.00	nd	nd	nd	0.06	0.00
S	0.04	0.03	0.05	0.01	0.04	40.15	34.83

[a] in contact with native nickel; bdl below detection limit; nd not determined

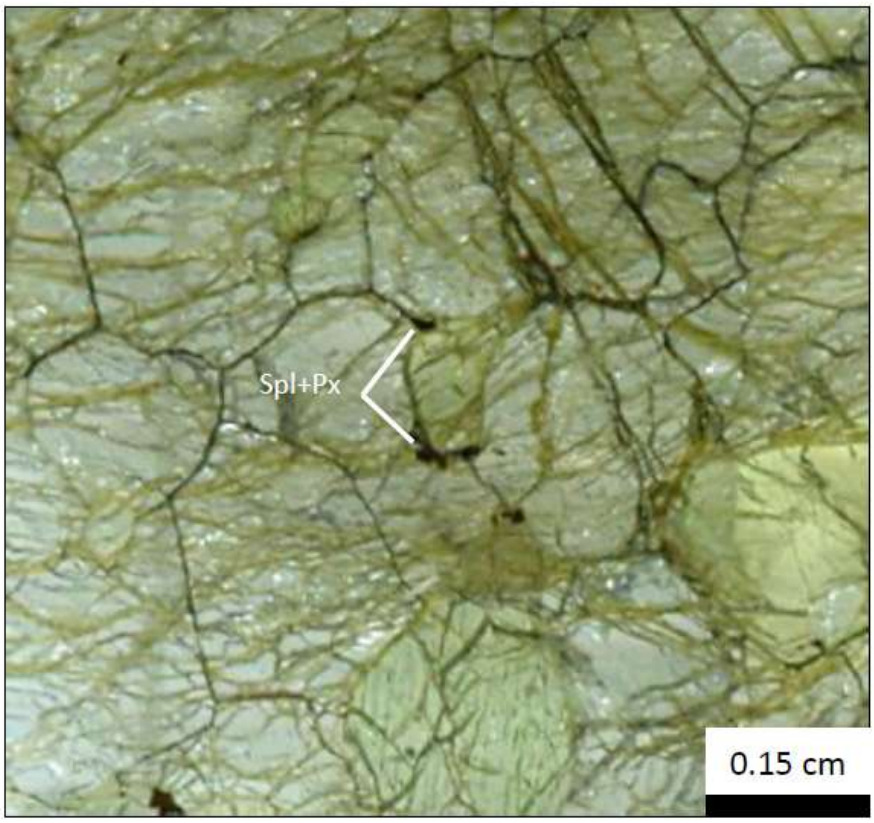

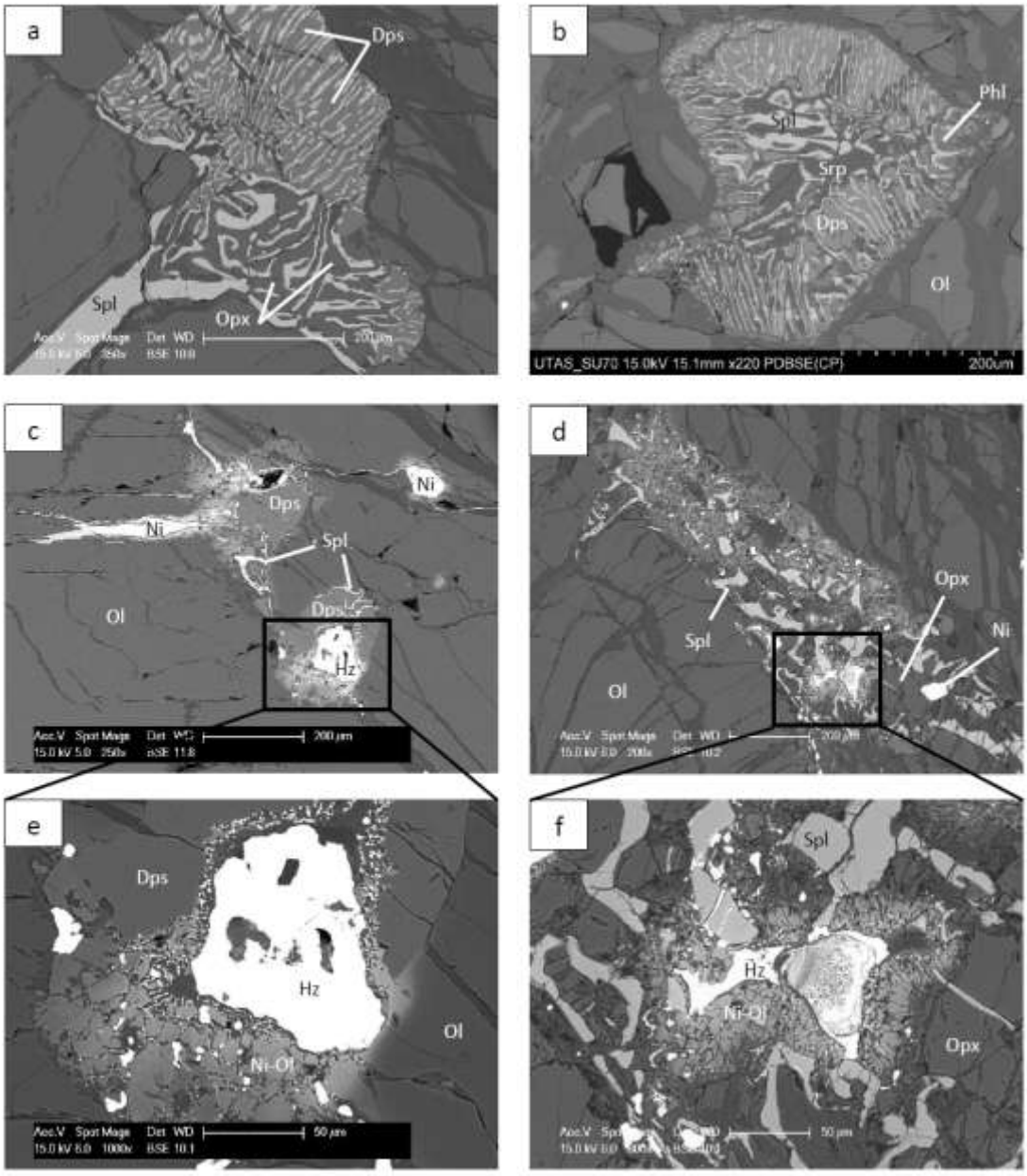
a
Dps
Spl
Opx
b
Phl
Spl
Srp
Dps
Ol
UTAS_SU70 15.0kV 15.1mm x220 PDBSE(CP)
200um
c
Ni
Dps
Ni
Spl
Ol
Dps
Hz
d
Opx
Spl
Ni
Ol
e
Dps
Hz
Ol
Ni-Ol
f
Spl
Hz
Ni-Ol
Opx

27

28

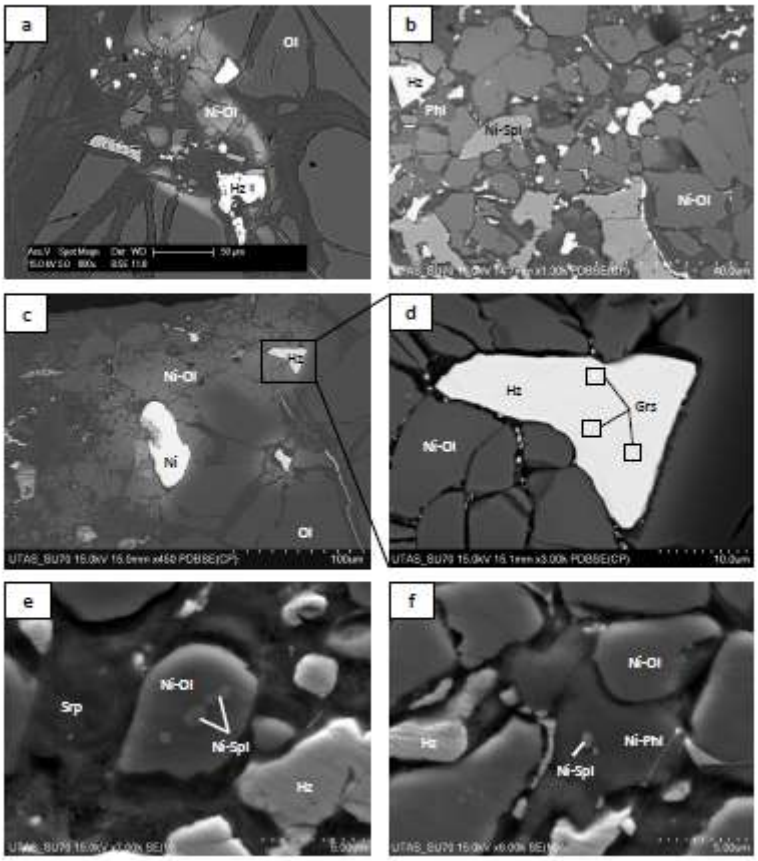
a
Ol
Ni-Ol
Hz
b
Hz
Phl
Ni-Spl
Ni-Ol
c
Hz
Ni-Ol
Ni
Ol
d
Hz
Grs
Ni-Ol
e
Ni-Ol
Srp
Ni-Spl
Hz
f
Ni-Ol
Hz
Ni-Phl
Ni-Spl

29

30

31

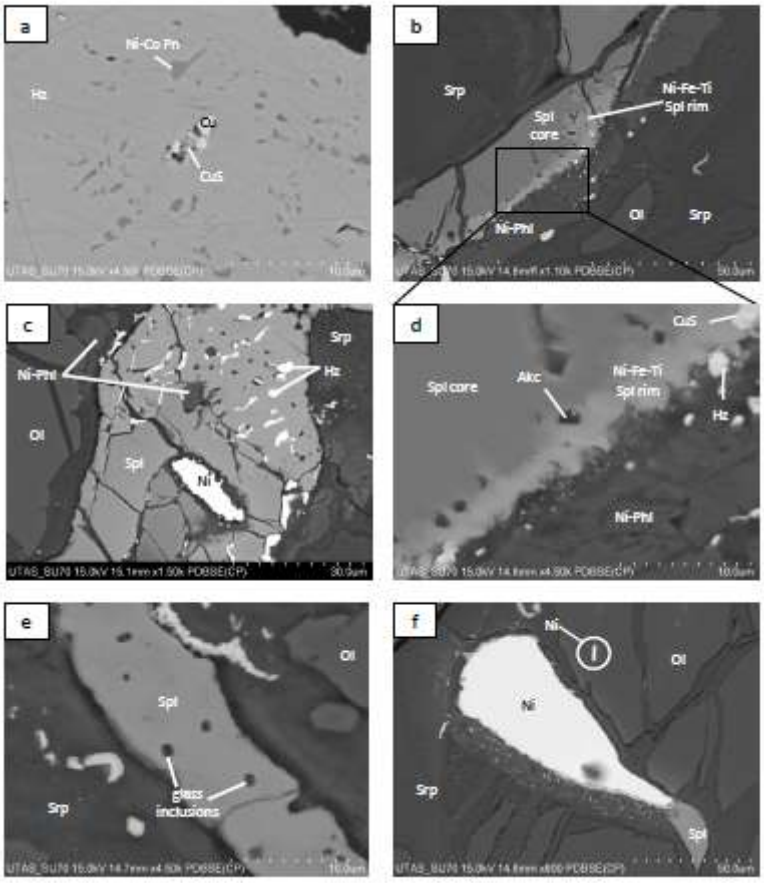

32

33

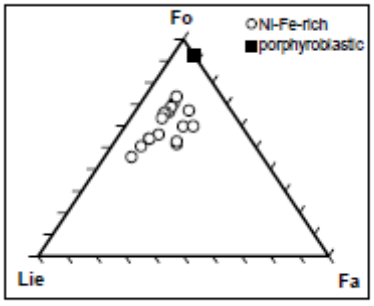

34

35

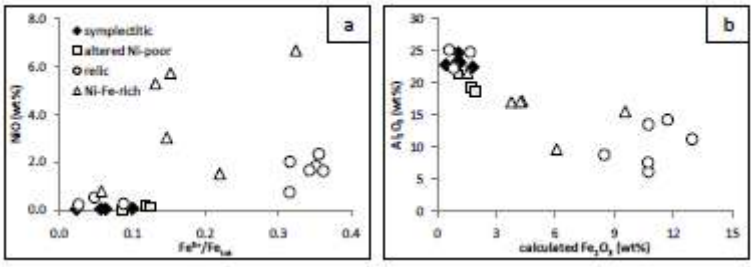

36

37

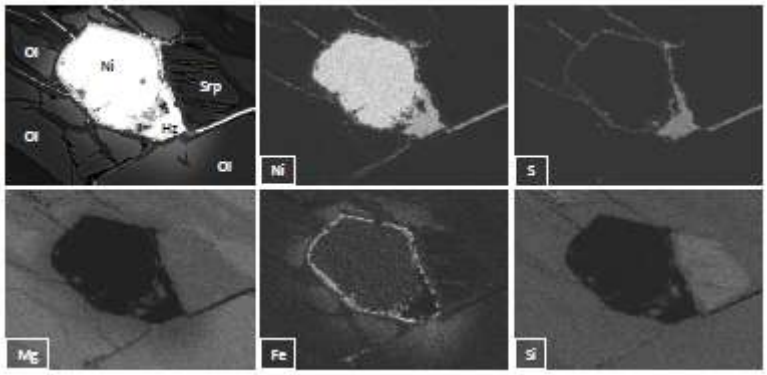
Ol
Ni
Srp
Hz
Ol
Ol
Ni
S
Mg
Fe
Si

38

39

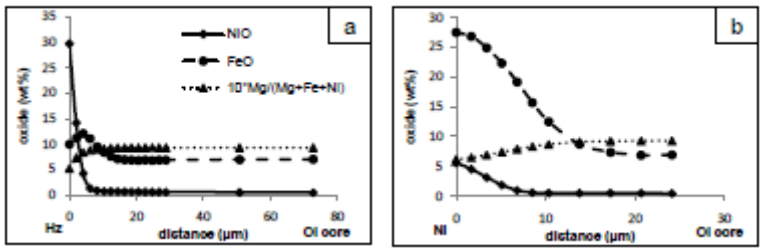
a
NiO
FeO
10*Mg/(Mg+Fe+Ni)
oxide (wt%)
distance (µm)
Hz
Ol core
b
oxide (wt%)
distance (µm)
Ni
Ol core

40

41

42